JAAS

Accepted Manuscript

ROYAL SOCIETY
OF **CHEMISTRY**

www.rsc.org/jaas

Calibration of single-particle inductively coupled plasma-mass spectrometry (SP-ICP-MS)

Wan-Waan Lee and Wing-Tat Chan*

Department of Chemistry, The University of Hong Kong, Pokfulam Road, Hong Kong SAR, PR China

Email address: wtchan@hku.hk; Tel: +852-2859-2156; Fax: +852-2857-1586

Abstract

We have identified incomplete particle vaporization and non-linear detector response as the major factors that cause non-linearity of SP-ICP-MS measurements at high particle mass. The contribution of incomplete vaporization to the deviation from linearity of the ICP-MS intensity is estimated using a mathematical model of particle vaporization. The non-linear detector response in the pulse-counting mode is due to overlapping of the analyte ions at the detector within the 40-ns dead time of the electron multiplier. The overlap can be severe because of the relatively short pulse duration of 300 μs of the ion plumes of the discrete sample particles. The non-linear detector response has been modeled using Poisson statistics.

We have also examined the applicability of calibration methods based on standard particles, discrete standard solution droplets, and continuous nebulization of standard solution. The standard-solution calibration method requires linear calibration curves. The method may also suffer from errors due to difference in sensitivity of the standard solution and sample particles. Calibration using standard particles and discrete standard solution droplets do not have the limitations.

1. Introduction

Single-particle inductively coupled plasma-mass spectrometry (SP-ICP-MS) is recognized as a convenient method for the determination of the elemental contents of nanoparticles [1-21]. Calibration of SP-ICP-MS intensity is straightforward, provided that a set of standard particles of suitable particle diameter is available. Degueldre *et al.* reported SP-ICP-MS calibration curves of Au nanoparticles [5]. The calibration curves were linear over the range of particle diameter of 80 – 200 nm. The curves rolled off at particle diameter of 250 nm. The SP-ICP-MS spike intensity in the linear range is directly proportional to the cube of the diameter of the particles. The linear dynamic range varies with the type of the sample particles. For particles of low density such as SiO_2, the linear range is 400 – 1800 nm [22, 23].

Calibration of SP-ICP-MS using standard particles, however, is limited by the availability of monodisperse standard particles that match the sample particles in thermal properties and particle diameter [24]. The standard particles must also be insoluble in water for successful calibration. Few monodisperse standard particles have been reported in the literatures. The reported standard particles include gold nanoparticles [5, 13, 25], silver nanoparticles [16, 19], and silicon dioxide particles [22, 23, 26]. A suitable set of standard particles is not always available. One-point calibration using polydisperse MgO particles of diameter of 100 nm have been used in the determination of the Mg contents of single-cell green algae [7] and bacteria [27].

Monodisperse droplets of standard solution have also been used successfully for SP-ICP-MS calibration [13, 22, 28-32]. Monodisperse droplets of wide range of dried analyte mass are readily prepared from standard solution of different concentration. The dried residues of the droplets are excellent surrogate of the standard particles. Garcia *et al.* [22] determined the mass of gold nanoparticles using single droplets of gold nanoparticle in gold standard solution for calibration. The relative error was < 2%. Gschwind *et al.* [13] studied the effectiveness of external calibration and internal calibration of Au, Ag and CeO_2 nanoparticles. In external calibration, droplets of standard solution and sample particles are introduced into the ICP independently. Difference in the matrix between the sample particles and the standard solutions results in calibration errors. Standard solution and the sample particle are contained in the same droplets in internal calibration. The matrix effects were reduced and the error in particle diameter was < 5%.

Calibration using continuous flow of aerosols of standard solutions is an alternative method for SP-ICP-MS [6, 10, 11, 20, 33-37]. The method has additional advantages over calibration with monodisperse droplets of standard solution in that a dedicated droplet generator is not required. The aerosols are generated using standard nebulizers for ICP-MS, such as concentric nebulizer [10, 11] and Micromist nebulizer [33-36]. The calibration method requires accurately known nebulization and transport efficiency which can be determined from the rate of the ICP-MS intensity spikes and the number density of a standard-particle suspension [7, 38]. The calibration curve of ICP-MS intensity *versus* concentration is converted into ICP-MS intensity *versus* mass flux of the analyte using the nebulization and transport efficiency. The principles of solution calibration are that (1) the ICP-MS intensity of a particle is directly proportional to the analyte contents of the particle and (2) the mass flux of the standard solution and the discrete sample particles can be compared directly. The first assumption requires linear calibration curve of the sample particles. However, the linear dynamic range of the calibration curves of standard particles is 1 to 2 orders of magnitude in particle diameter [5, 9, 13, 16, 19, 22, 23, 25, 28-30, 39] and approximately 3 orders of magnitude in mass only. For example, the linear range of particle diameter of gold nanoparticle is 20 – 200 nm [5, 39]. The calibration curve rolls off at high mass [5, 8, 16, 19, 22, 23, 28]. The applicable particle-mass range of solution calibration is relatively limited. In contrast, calibration using standard particles or solution droplets in the nonlinear range is possible. Standard particles of similar analyte mass as the sample particles will have the same relationship of ICP-MS intensity *versus* analyte quantity. Calibration using discrete standard droplets or particles, therefore, can be extended to the non-linear range of the calibration curve.

The second assumption of standard-solution calibration requires that the rates of particle vaporization and diffusion in the ICP are the same for the sample particles and the standard solution aerosols. However, the dried residues of the standard-solution aerosols are relatively small and the number of aerosols in the ICP is large. The rates of particle vaporization and analyte diffusion of the standard-solution aerosols are likely different from the sample particles. The errors by solution calibration are indeed relatively large [6, 11, 18, 20, 33]. The diameter of the 100-nm silver nanoparticles was underestimated by 20% [20]. Since the mass of a particle is directly proportional to the cube of its diameter, the particle mass is underestimated by 50% or more. We have similar observation of calibration error of -74% in the determination of the Mg contents of single-cell algae using standard-solution calibration [18]. The large error is likely due to fast diffusion loss of the low-mass Mg atoms from the ion plumes of the algal cells. Using polydisperse MgO particles for calibration, the error was reduced to 6%. The standard particles probably have similar Mg diffusion loss as the biological cells in the ICP and are, therefore, better calibration standard than the standard solution.

An additional precaution of standard-solution calibration for SP-ICP-MS is that the instantaneous count rate of the sample plume can be very large and exceed the linear range of digital pulse-counting mode of the ICP-MS detector. Deviation of the measured ICP-MS intensity from linearity increases as particle mass and intensity increases. We will show that the linear dynamic range of SP-ICP-MS is limited to 3 orders of magnitude because of non-linear detector response. The linear range is significantly lower than the range of 6 orders of magnitude for solution sample measurement. Liu *et al.* [39] recently reported that the linear range in the high particle-mass range could be extended by reducing the sensitivity of the detector.

In this study, two major factors that determine the linearity of SP-ICP-MS calibration curves will be discussed. These factors are the degree of vaporization of the sample particles and linearity of detector response in pulse-counting mode. Gold nanoparticles will be used as model particles in the discussion. Experimental measurement of SP-ICP-MS intensity of standard gold nanoparticles and computer simulation of particle vaporization will be presented. The mathematical model will also be used to show the relationship of linear dynamic range of a calibration curve and the particle properties. There are few discussions on the suitable ICP operating conditions for the SP-ICP-MS measurements. Operating conditions of the ICP for solution samples are often used. Studying the linearity of single-particle ICP-MS calibration curves and the ICP-MS depth profiles against the ICP operating conditions may provide useful information for the selection of experimental parameters for SP-ICP-MS measurements.

2. Experimental

2.1 Chemical and solutions

Gold nanoparticle suspensions (British Biocell International, Cardiff, UK) of nominal particle diameter of 60 nm, 80 nm, 100 nm, 150 nm, and 250 nm (coefficient of variation CV $\leq$ 8%) were used in this study. The gold nanoparticle suspensions were diluted to approximately 10^4/mL using deionized water before ICP-MS measurement.

Aqueous gold standard for ICP (1000 μg/mL Trace CERT®, Fluka, Seelze, Germany) was used to prepare standard solution for calibration. The stock solution was diluted using deionized water to 2 – 200 ng/mL prior to use.

2.2 ICP-MS measurement

A quadrupole-based inductively coupled plasma-mass spectrometer (Agilent 7500a, Agilent Technologies, CA, USA) was used in this study. The general ICP-MS operating parameters are shown in Table 1. The instrument was tuned using an aqueous multi-element standard solution, which contained 10 ng/mL each of Li, Y, Co, Ce and Tl, for consistent sensitivity (^{7}Li, ^{89}Y and ^{205}Tl) and minimum level of doubly-charged ions and oxide species (^{140}Ce) before each experiment.

A V-groove nebulizer and a water-cooled Scott-type double-pass spray chamber (temperature = 2 °C) were used for aerosol generation. The particle suspension was introduced into the nebulizer using a syringe pump (NE-1000 Single Syringe Pump, New Era Pump Systems, NY, USA).

The spectrometer was operated in time-resolved analysis (TRA) mode. The minimum integration time of 10 ms was used to minimize the chance of particle overlap in the integration window. The duration of each measurement was typically 60 s. Only one mass-to-charge ratio (m/z) can be monitored in the TRA measurement. The isotope ^{197}Au was measured.

3. Results and discussion

Calibration curves of gold nanoparticles of diameter of 60 – 250 nm were constructed for ICP forward power of 1200 and 1400 W and sampling depth of 4 to 8 mm. The linear range of the calibration curves and the deviation from linearity of the large gold nanoparticles are correlated with the degree of particle vaporization. Correction factor for non-linear response of the ICP-MS detector is calculated for the estimation of the deviation due to incomplete particle vaporization.

3.1 Calibration curves of gold nanoparticles

Figure 1a shows the temporal ICP-MS intensity profile of ^{197}Au for the 100-nm gold nanoparticles. The ICP-MS intensity spikes were binned to give the distribution of ICP-MS intensity (Figure 1b). The intensity distribution is approximately log-normal. The peak maximum of the intensity distribution of the 100-nm gold nanoparticles is 2.44 (280 counts). The rate of the ICP-MS intensity spikes is 5.4 Hz

(Figure 1a). The probability of spikes due to overlapping of 2 particles within the 10-ms integration window is approximately 3% by Poisson statistics [26]. The error for the estimation of the peak maximum of the distribution due to spike overlapping is negligible. The peak maximum of the intensity distribution is the median intensity of the population [40]. The median intensity is within 2% of the trimmed mean (5% trim). The peak maximum will be used in the construction of the calibration curves.

Calibration curves of gold nanoparticles of diameter of 60, 80, 100, 150 and 250 nm were constructed for sampling depth of 4 to 8 mm in 0.5 mm increment for ICP forward power of 1200 W and 1400 W and central channel gas flow rate of 1.05 L/min. Calibration curves at sampling depth of 7 and 12 mm for ICP forward power of 1400 W and central channel gas flow rate of 0.95 L/min were also constructed and shown in Figure 2. All calibration curves are linear for gold nanoparticles of diameter of 60 – 150 nm. The calibration curves roll off at high mass. The intensity of the 250-nm particle deviates negatively from linearity for all experimental conditions. The linear range of the calibration curves is limited. The deviation from linearity of the 250-nm gold nanoparticles over a wider range of sampling depth and gas flow rate will be estimated from the intensity of the 100-nm particles in the Section 3.3.

3.2 Calibration using standard solution

The calibration curves of gold nanoparticles of diameter ≤150 nm are linear for all experimental conditions. The linear curves indicate that the particles (60–150 nm) are completely vaporized at the sampling depth studied. Using our mathematical model [8], the calculated degree of vaporization of the 100-nm gold nanoparticles is

>95% at sampling depth of 4 mm. The completely vaporized particles in fact have the same sampling depth profile as the standard solution (concentration range 2 to 200 ppb of Au). The normalized sampling depth profiles of the 100-nm gold nanoparticles and the Au standard solution are nearly identical (Figure 3). Solution calibration of SP-ICP-MS measurement of gold nanoparticles of diameter ≤150 nm seems feasible within the limited linear mass range. However, successful calibration also requires that the sensitivity of the standard solution and the sample particles are the same.

The sensitivity of a particle can be calculated by dividing the ICP-MS intensity of the particle by the number of atoms in the particle. The number of atoms is estimated from the diameter of the gold nanoparticle and the density of gold (19.3 g/cm^3 [41]), assuming a spherical particle. The sensitivity of the 100-nm gold nanoparticles is 7.30×10^{-6} count/atom at sampling depth of 6 mm.

The sensitivity of the standard solution is calculated from the mass flux of the analyte introduced into the ICP. The nebulization and transport efficiency of the sample introduction system must be determined accurately for the mass-flux estimation [7, 38]. The nebulization and transport efficiency ε can be estimated by counting the number of spikes N_s observed over the measurement duration t for a standard particle suspension of particle number density N and sample uptake rate V.

$$N_s = N \times V \times t \times \varepsilon \qquad (1)$$

The assumption of same nebulization and transport efficiency of the discrete particles and standard solution is valid for particles of diameter of a few micrometer or less [42, 43]. The nebulization and transport efficiency is 2.1% for the current experimental setup. The sensitivity of the standard solution is 1.30×10^{-5} count/atom for integration window of 10 ms. The solution sensitivity is, on average, 1.7 times larger than the particle sensitivity over the range of sampling depth of 4 to 14 mm. The lower sensitivity of the 100-nm gold nanoparticles is likely due to larger diffusion loss of the discrete particles compared to the aerosols of the standard solution [7, 8]. Solution calibration will result in relative error of -40% in mass and -17% in diameter. An additional empirical correction factor is required for solution calibration. The empirical factor can be established by comparing the intensity of a standard particle that is known to be completely vaporized (*e.g.*, the 100-nm gold nanoparticle in this study) and the intensity of the standard solution of the same mass flux.

Table 2 shows the errors in particle diameter and analyte contents reported in the literature. The errors are generally smaller for calibration using single standard-solution droplets and standard particles compared to solution calibration. Solution calibration for the determination of analyte contents is semi-quantitative.

3.3 Nonlinear calibration curve due to incomplete vaporization

Incomplete vaporization of the large sample particles in the ICP is inevitable [8, 22, 23, 44-49]. For example, the calibration curve of SiO_2 is linear for particle diameter of 400 nm to 1 μm at ICP forward power of 1300 W and central channel gas flow rate of 0.8 – 0.9 L/min. The calibration curve rolls off at particle diameter ≥800 nm at central channel gas flow rate of 1.0 L/min [23]. The negative deviation from linearity for ICP-MS intensity of the 250-nm gold nanoparticles in Figure 2 is partly due to incomplete vaporization of the particles. (The other factor of non-linear detector response will be discussed in the next section). The deviation is -36% and -15% for sampling depth of 7 mm and 12 mm, respectively. The deviation reduces as sampling depth increases, probably because of longer residence time at the higher sampling position and thus higher degree of vaporization.

From the study in Section 3.1, the 100-nm gold nanoparticles are within the linear calibration curves for a wide range of sampling depth. The intensity of the 100-nm gold nanoparticles will be used to estimate the deviation from linearity of the ICP-MS intensity of the 250-nm gold nanoparticles. The degree of vaporization of the 100-nm gold nanoparticles is calculated to be >95% at sampling depth of 4 mm using our mathematical model [8] (Figure 4). The 100-nm particle will be assumed to have completely vaporized in the range of sampling depth studied (4 to 14 mm) in the following paragraphs.

Mathematical model [8] is used to calculate the degree of particle vaporization to facilitate discussion of the relative error in calibration due to incomplete particle vaporization. The calculation of the rate constants of particle vaporization is based on the combination of heat-transfer and mass-transfer-limited vaporization rate models [50-52]. The ICP conditions for the simulation in Figure 4 are: ICP forward power = 1400 W, central channel gas flow rate = 1.05 L/min, evaporation coefficient = 0.03, linear gas temperature profile of 500 K/mm [51, 52].

Figure 4 shows the simulation results of degree of vaporization of 100-nm and 250-nm gold nanoparticles. At sampling depth of 4 mm, the degree of vaporization of the 100-nm gold nanoparticles is >95%, while that of the 250-nm particle is only

60%. The 100-nm particles are 100% vaporized at sampling depth of 6 mm, compared to 75% of the 250-nm particles. The deviation from linearity of ICP-MS intensity of the 250-nm gold nanoparticles can be estimated from the difference in the degree of vaporization of the 100-nm and 250-nm particles (Figure 5). The deviation reduces as the sampling depth increases because of increase in the duration of time for particle vaporization. It should be noted that diffusion of the analyte atoms has not been considered in the above discussion for simplicity. The deviation is expected to be less severe if diffusion loss is considered in the simulation.

The measured depth profiles of ICP-MS intensity of 100-nm and 250-nm gold nanoparticles at forward power of 1400 W and central channel gas flow rate of 1.05 L/min are shown in Figure 6. The ICP-MS intensity depth profile of the 100-nm particle is used to calculate the theoretical depth profile of the 250-nm particles, assuming complete vaporization (Figure 6b). The relative difference of the experimental depth profile and theoretical depth profile is shown in Figure 6c. The relative deviation from linearity reduces as the sampling depth increases, in agreement of the vaporization model (Figure 5). The relative deviations from 5 to 10 mm, however, are larger than the theoretical deviation based on particle vaporization. The degree of particle vaporization is not the only factor affecting the linearity of the calibration curve. As mentioned in the preceding paragraph, diffusion is not considered in the vaporization calculation. Diffusion loss of the analyte ions is expected to be more severe for the smaller particles that have completed vaporization at low sampling position. The relative deviation from linearity for the larger particles will be reduced because of the difference in diffusion loss. The larger than expected deviations in Figure 6 is not related to analyte diffusion, but is probably related to non-linear detector responses of the transient intensity of the single particles.

3.4 Non-linear detector response of the transient intensity

In SP-ICP-MS, digital ion-counting mode of detection is used because of the relatively small ICP-MS intensity of the nanoparticles. For example, the largest ICP-MS intensity in Figure 2a is approximately 3000 counts for the 250-nm gold nanoparticles. The intensity is integrated over 10 ms. The average count rate is 3×10^5 count/s, well within the limit of 1×10^6 count/s for linear response of an electron multiplier in pulse counting mode [23]. However, the full-width-at-half-maximum of an ion plume is approximately 300 μs [12, 23, 53-55]. The instantaneous ion rate at the detector can be much higher than the linear dynamic range of the detector and non-linear response of the detector occurs. Figure 7 shows the count rate of a hypothetical Gaussian pulse of base width of 600 μs. The ideal total count of the pulse is 1000 counts. The count rate of a steady signal (e.g., standard solution) that gives 1000 counts over the 10-ms integration window is also shown for comparison. The count rate at the peak of the Gaussian pulse is approximately 48 times that of the count rate of the steady signal, 4.8×10^6 and 1×10^5 count/s, respectively. The count rate of the pulse at the peak already exceeds the linear dynamic range of the detector.

The ions enter the detector randomly. The deviation from linearity of the detector response can be estimated using Poisson statistics. The probability of finding k ions within the observation window of the detector in pulse-counting mode, $P(k,\lambda)$, is given below [26].

$$P(k,\lambda) = \frac{\lambda^k e^{-\lambda}}{k!} \tag{2}$$

where λ is the chance of occurrence of an ion within the observation window, e is the base of natural logarithm. The observation window is assigned as the dead time of the electron multiplier (40 ns) [56]. The instantaneous count rate of the Gaussian pulse is calculated from the sum of $P(k,\lambda)$ for k = 1, 2, 3, and 4 (Figure 7). The total count is 930 counts instead of 1000 because of overlapping of the analyte ions at the detector. The deviation from linearity is -7% due to non-linear detector response. The simulation is repeated for ideal ion counts of 100 – 4000 and the relative errors are shown in Figure 8. The relative error increases with count rate. The error is substantial (>10%) at 1500 counts or more. The relative error for the steady signal is negligible because of the relatively low count rate.

The above simulation is relatively crude. The temporal ICP-MS intensity profile of an ion plume is represented by a Gaussian peak. Correction factors derived from the results in Figure 8 are approximate. The measured intensity of the 250-nm particles in Figure 6b is corrected using the simulation results in Figure 8. The deviation from linearity is reduced (Figure 9) and is comparable to the theoretical deviation in Figure 5. The deviation reduces from -34% to -20% and -12% to -1% at sampling depth of at 6 and 10 mm, respectively. The degree of vaporization of the 250-nm particles is >95% at sampling depth of 12 mm (Figure 4). The deviation from linearity due to incomplete vaporization is negligible at this sampling depth. The deviation becomes positive at sampling depth >12 mm probably because of more severe diffusion loss of the 100-nm particles as the particles finish vaporization earlier than the 250-nm particles.

It is interesting to note that, for ICP forward power of 1400 W and central channel gas flow rate of 0.95 L/min, the estimated position of complete vaporization of the 250-nm gold nanoparticle is 12 mm using the empirical equation of our previous study [8]. The deviation from linearity of the 250-nm gold nanoparticles in Figure 2b is -15%. The deviation reduces to -3% with the correction of the detector response. The deviation in Figure 2a for sampling depth of 7 mm is -35% and is reduced to -16% with detector-response correction. Incomplete vaporization of the large particles occurs at sampling depth of 7 mm. For successful solution calibration, the sampling depth must be larger than 12 mm in order to obtain a linear calibration curve for the sample particles.

Correction of the detector response has also been applied to the study of the deviation from linearity of the 250-nm particles *versus* central channel gas flow rate. The intensity of both the 100-nm and 250-nm particles increases with gas flow rate from 0.75 L/min to 0.85 L/min. The intensity reduces at higher gas flow rate (Figures 10a and 10b). The deviation from linearity increases from 0.75 to 0.85 L/min and is relatively constant from 0.90 to 1.05 L/min (Figure 10c). It is noted that the maximum intensity of the 250-nm gold nanoparticles at 0.85 L/min is 4000 counts (Figure 10b), at which the deviation from linearity is the greatest (Figure 10c). The intensity is large and significant non-linear response of the detector is expected (Figure 8). After the correction of non-linear detector response, the profile of deviation from linearity changes completely (Figure 10c *versus* Figure 11). The corrected profile agrees with the model that the degree of vaporization is higher at lower central channel gas flow rate due to longer residence time of particles in plasma. The starting position of particle vaporization is also shifted upstream of the plasma at lower gas flow rate [52].

The deviation from linearity, therefore, decreases as central channel gas flow rate decreases.

4. Simulated calibration curves

In the last section, we show that the linearity of a calibration curve is related to the degree of vaporization of the large particles. In the heat-transfer and mass-transfer-limited vaporization mechanisms, the vaporization rate depends on the molecular weight of the analyte and the density of the particle [50-52]. The boiling point determines the starting position of particle vaporization in the ICP. To illustrate the effects of density, molecular weight, and boiling point on the linearity of a calibration curve, the intensity of SiO_2, PbO, and Yb_2O_3 are calculated using the mathematical model [8]. The properties of the model particles are listed in Table 3. The diameters of the particles are 60, 80, 100, 150, 200, and 250 nm, in parallel with the Au nanoparticles. The ICP operating conditions are ICP forward power = 1400 W, central channel gas flow rate = 1.05 L/min, and sampling depth = 4 mm. The same gas temperature gradient in Section 3.3 is used.

The simulated calibration curves are shown in Figure 12. SiO_2 has slightly higher boiling point than gold nanoparticles. The density is approximately 1/7 of gold. The molecular weight is approximately 1/3 of Au. The simulated calibration curve of SiO_2 is linear at sampling depth of 4 mm (Figure 12a). PbO has high molecular weight and relatively high density. However, the boiling point of PbO is low. PbO starts vaporization much earlier than gold. At sampling depth of 4 mm, the degree of vaporization of the 250-nm PbO particles is 100%. The simulated calibration curve of PbO is also linear at 4 mm. Yb_2O_3 has relatively high density and the largest molecular weight and boiling point among the particles. Yb_2O_3 starts vaporization later than gold. The degree of vaporization of the 150-nm particles is only 80% at sampling depth of 4 mm. The simulated calibration curve of Yb_2O_3 deviates from linearity for particle diameter ≥150 nm at sampling depth of 4 mm. The linear range for the high-boiling particles is limited.

The linearity of the calibration curve depends strongly on the particle properties. Particles of low density, molecular weight, and boiling point vaporize at higher rate and will likely give linear calibration curves. Solution calibration for these particles is expected to be more successful.

5. Conclusions

We have identified incomplete particle vaporization and non-linear detector response in the pulse counting mode as two major causes of non-linear calibration curves at high particle mass. Linear calibration curves are desirable for SP-ICP-MS measurement, especially for solution calibration. The calibration curves for particles of low density, low molecular weight, and low boiling point are more likely linear over a wide range of particle diameter. For particles that do not vaporize rapidly, measurement at higher sampling positions and use of higher forward power and lower central channel gas flow may extend the linear range of the calibration curves. Calibration using standard particles and single droplets of standard solution is less susceptible to calibration errors if the sample particles and the standard particles are similar in mass.

Experimental conditions that give high sensitivity are preferred for the measurement of small particles that are close to the measurement limits. The sensitivity can be increased by increasing the power or decreasing the central channel gas flow rate. The curve may become nonlinear in the high mass range because of non-linear detector response for spike intensity larger than 1000 counts in the pulse-counting mode. Linear calibration at the high mass range can be obtained by reducing the sensitivity of the measurement. However, since the linear dynamic range is 3 orders of magnitude in mass and 1 order in particle diameter only, reducing the sensitivity will result in increase of the detection limits, *i.e.*, the smaller particles will not be detected. The linear range can also be extended by correction of the non-linear detector response (Figure 8). However, detailed characterization of the temporal ICP-MS intensity profile of the ion plumes is needed. Solution calibration is more susceptible to the non-linear detector response than standard particle calibration. Correction of detector response may not be necessary for standard particle and standard droplet calibration if the mass of the sample particle and the standard particles are similar.

Experimental data from the literatures show that standard-solution calibration is semi-quantitative. The error is generally negative because of low sensitivity of the sample particles compared to the standard solution. An empirical correction factor is needed for standard-solution calibration.

Acknowledgments

This work was supported by a grant from the Research Grant Council of the Hong Kong Special Administrative Region, China (Project No. 17300414) and the Seed Funding Programme for Basic Research of The University of Hong Kong.

References

1. C. Degueldre and P. Y. Favarger, *Colloids and Surfaces A: Physicochemical and Engineering Aspects*, 2003, **217**, 137-142.
2. C. Degueldre and P. Y. Favarger, *Talanta*, 2004, **62**, 1051-1054.
3. C. Degueldre, P. Y. Favarger and C. Bitea, *Analytica Chimica Acta*, 2004, **518**, 137-142.
4. C. Degueldre, P. Y. Favarger, R. Rossé and S. Wold, *Talanta*, 2006, **68**, 623-628.
5. C. Degueldre, P. Y. Favarger and S. Wold, *Analytica Chimica Acta*, 2006, **555**, 263-268.
6. Y. Suzuki, H. Sato, S. Hikida, K. Nishiguchi and N. Furuta, *Journal of Analytical Atomic Spectrometry*, 2010, **25**, 947-949.
7. K. S. Ho and W. T. Chan, *Journal of Analytical Atomic Spectrometry*, 2010, **25**, 1114-1122.
8. K.-S. Ho, K.-O. Lui, K.-H. Lee and W.-T. Chan, *Spectrochimica Acta Part B: Atomic Spectroscopy*, 2013, **89**, 30-39.
9. S. Kaneco, T. Nomizu, T. Tanaka, N. Mizutani and H. Kawaguchi, *Analytical Sciences*, 1995, **11**, 835-840.
10. F. Li, D. W. Armstrong and R. S. Houk, *Analytical Chemistry*, 2005, **77**, 1407-1413.
11. Y. Suzuki, H. Sato, K. Hiyoshi and N. Furuta, *Spectrochimica Acta Part B: Atomic Spectroscopy*, 2012, **76**, 133-139.
12. S. Gschwind, L. Flamigni, J. Koch, O. Borovinskaya, S. Groh, K. Niemax and D. Gunther, *Journal of Analytical Atomic Spectrometry*, 2011, **26**, 1166-1174.
13. S. Gschwind, H. Hagendorfer, D. A. Frick and D. Günther, *Analytical Chemistry*, 2013, **85**, 5875-5883.
14. F. Laborda, E. Bolea and J. Jiménez-Lamana, *Analytical Chemistry*, 2013.
15. F. Laborda, E. Bolea and J. Jiménez-Lamana, *Analytical Chemistry*, 2014, **86**, 2270-2278.
16. F. Laborda, J. Jimenez-Lamana, E. Bolea and J. R. Castillo, *Journal of Analytical Atomic Spectrometry*, 2011, **26**, 1362-1371.
17. F. Laborda, J. Jimenez-Lamana, E. Bolea and J. R. Castillo, *Journal of Analytical Atomic Spectrometry*, 2013, **28**, 1220-1232.
18. D. Drescher, C. Giesen, H. Traub, U. Panne, J. Kneipp and N. Jakubowski, *Analytical Chemistry*, 2012, **84**, 9684-9688.
19. B. Franze, I. Strenge and C. Engelhard, *Journal of Analytical Atomic*

Spectrometry, 2012, **27**, 1074-1083.

20. D. M. Mitrano, A. Barber, A. Bednar, P. Westerhoff, C. P. Higgins and J. F. Ranville, *Journal of Analytical Atomic Spectrometry*, 2012, **27**, 1131-1142.
21. D. M. Mitrano, E. K. Lesher, A. Bednar, J. Monserud, C. P. Higgins and J. F. Ranville, *Environmental Toxicology and Chemistry*, 2012, **31**, 115-121.
22. C. C. Garcia, A. Murtazin, S. Groh, V. Horvatic and K. Niemax, *Journal of Analytical Atomic Spectrometry*, 2010, **25**, 645-653.
23. J. W. Olesik and P. J. Gray, *Journal of Analytical Atomic Spectrometry*, 2012, **27**, 1143-1155.
24. K.-S. Ho, Ph. D. Thesis, The University of Hong Kong, 2012.
25. S. A. Pergantis, T. L. Jones-Lepp and E. M. Heithmar, *Analytical Chemistry*, 2012, **84**, 6454-6462.
26. A. Murtazin, S. Groh and K. Niemax, *Journal of Analytical Atomic Spectrometry*, 2010, **25**, 1395-1401.
27. C.-N. Tsang, K.-S. Ho, H. Sun and W.-T. Chan, *Journal of the American Chemical Society*, 2011, **133**, 7355-7357.
28. T. Nomizu, H. Hayashi, N. Hoshino, T. Tanaka, H. Kawaguchi, K. Kitagawa and S. Kaneco, *Journal of Analytical Atomic Spectrometry*, 2002, **17**, 592-595.
29. T. Nomizu, S. Kaneco, T. Tanaka, D. Ito, H. Kawaguchi and B. T. Vallee, *Analytical Chemistry*, 1994, **66**, 3000-3004.
30. T. Nomizu, S. Kaneco, T. Tanaka, T. Yamamoto and H. Kawaguchi, *Analytical Sciences*, 1993, **9**, 843-846.
31. T. Nomizu, H. Nakashima, Y. Hotta, T. Tanaka and H. Kawaguchi, *Analytical Sciences*, 1992, **8**, 527-531.
32. H. Kawaguchi, N. Fukasawa and A. Mizuike, *Spectrochimica Acta Part B: Atomic Spectroscopy*, 1986, **41**, 1277-1286.
33. H. E. Pace, N. J. Rogers, C. Jarolimek, V. A. Coleman, E. P. Gray, C. P. Higgins and J. F. Ranville, *Environmental Science & Technology*, 2012, **46**, 12272-12280.
34. J. Tuoriniemi, G. Cornelis and M. Hassellöv, *Analytical Chemistry*, 2012, **84**, 3965-3972.
35. S. T. Kim, H. K. Kim, S. H. Han, E. C. Jung and S. Lee, *Microchemical Journal*, 2013, **110**, 636-642.
36. J. Tuoriniemi, G. Cornelis and M. Hassellov, *Journal of Analytical Atomic Spectrometry*, 2014, **29**, 743-752.
37. K.-O. Lui, Ph. D. Thesis, The University of Hong Kong, 2011.
38. H. E. Pace, N. J. Rogers, C. Jarolimek, V. A. Coleman, C. P. Higgins and J. F.

Ranville, *Analytical Chemistry*, 2011, **83**, 9361-9369.

39. J. Liu, K. E. Murphy, R. I. MacCuspie and M. R. Winchester, *Analytical Chemistry*, 2014, **86**, 3405-3414.
40. E. Limpert, W. A. Stahel and M. Abbt, *BioScience*, 2001, **51**, 341-352.
41. D. R. Lide, ed., *CRC handbook of chemistry and physics*, 79th edn., CRC Press LLC, Boca Raton,, 1998.
42. K. J. Jankowski and E. Reszke, *Microwave induced plasma analytical spectrometry*, RSC Pub, Cambridge, 2011.
43. A. Montaser, ed., *Inductively coupled plasma mass spectrometry*, J. Wiley, New York, 1998.
44. A. Murtazin, S. Groh and K. Niemax, *Spectrochimica Acta Part B: Atomic Spectroscopy*, 2012, **67**, 3-16.
45. L. Flamigni, J. Koch, H. Wiltsche, R. Brogioli, S. Gschwind and D. Gunther, *Journal of Analytical Atomic Spectrometry*, 2012, **27**, 619-625.
46. C. C. Garcia, H. Lindner and K. Niemax, *Journal of Analytical Atomic Spectrometry*, 2009, **24**, 14-26.
47. H.-R. Kuhn, M. Guillong and D. Günther, *Analytical and Bioanalytical Chemistry*, 2004, **378**, 1069-1074.
48. M. Guillong and D. Gunther, *Journal of Analytical Atomic Spectrometry*, 2002, **17**, 831-837.
49. R. S. Houk, R. K. Winge and X. Chen, *Journal of Analytical Atomic Spectrometry*, 1997, **12**, 1139-1148.
50. J. A. Horner and G. M. Hieftje, *Spectrochimica Acta Part B: Atomic Spectroscopy*, 1998, **53**, 1235-1259.
51. J. A. Horner, S. A. Lehn and G. M. Hieftje, *Spectrochimica Acta Part B: Atomic Spectroscopy*, 2002, **57**, 1025-1042.
52. J. A. Horner, G. C. Y. Chan, S. A. Lehn and G. M. Hieftje, *Spectrochimica Acta Part B: Atomic Spectroscopy*, 2008, **63**, 217-233.
53. M. H. P. Yau and W.-T. Chan, *Journal of Analytical Atomic Spectrometry*, 2005, **20**, 1197-1202.
54. S. Groh, C. C. Garcia, A. Murtazin, V. Horvatic and K. Niemax, *Spectrochimica Acta Part B: Atomic Spectroscopy*, 2009, **64**, 247-254.
55. L. Flamigni, J. Koch and D. Günther, *Spectrochimica Acta Part B: Atomic Spectroscopy*, 2012, **76**, 70-76.
56. Agilent, personal communication, October 29, 2014.

List of Figures

Figure	
1	(a) ICP-MS temporal profile of ^{197}Au of the 100-nm gold nanoparticles. (b) ICP-MS intensity distribution of the particles. (ICP forward power = 1400 W, central channel gas flow rate = 1.05 L/min, sampling depth = 6 mm, particle number density = 10^4/mL).
2	Calibration curves of gold nanoparticles of diameter of 60, 80, 100, 150 and 250 nm at sampling depth (a) 7 mm and (b) 12 mm. Forward power = 1400 W and central channel gas flow rate = 0.95 L/min.
3	Depth profiles of normalized intensity of gold standard solution and 100-nm gold nanoparticles. (ICP forward power = 1400 W, central channel gas flow rate = 1.05 L/min).
4	Degree of vaporization against sampling depth for the 100-nm and 250-nm gold nanoparticles. (ICP forward power = 1400 W, central channel gas flow rate = 1.05 L/min).
5	Relative error in calibration due to incomplete vaporization of the 250-nm gold nanoparticle. (ICP forward power = 1400 W, central channel gas flow rate = 1.05 L/min).
6	Depth profiles of ICP-MS intensity of (a) 100-nm and (b) 250-nm gold nanoparticles. (c) Relative deviation from linearity of ICP-MS intensity of the 250-nm gold nanoparticles. (ICP forward power = 1400 W, central channel gas flow rate = 1.05 L/min).
7	Simulated ideal and suppressed count rates for transient signal of base width of 600 μs and continuous steady signal. Both signals give 1000 counts in the 10-ms integration window. The dead time of the electron multiplier is 40 ns.
8	Relative error of the ICP-MS detector operated in digital pulse-counting mode *versus* the intensity of the 600-μs Gaussian transient signal in Figure 7.
9	Corrected deviation of ICP-MS intensity of the 250-nm gold nanoparticles. (ICP forward power = 1400 W, central channel gas flow rate = 1.05 L/min).
10	Profiles of SP-ICP-MS intensity *versus* central channel gas flow rate of (a) 100-nm and (b) 250-nm gold nanoparticles. (c) Deviation from linearity of ICP-MS intensity of the 250-nm gold nanoparticles. (ICP forward power = 1400 W, sampling depth = 7 mm).
11	Corrected deviation of ICP-MS intensity of the 250-nm gold nanoparticles *versus* central channel gas flow rate. (ICP forward power = 1400 W,

sampling depth = 7 mm).

12 Simulated calibration curves of nanoparticles of (a) SiO_2, (b) PbO and (c) Yb_2O_3. ICP forward power = 1400 W, central channel gas flow rate = 1.05 L/min, and sampling depth = 4 mm. Particle diameter = 60, 80, 100, 150, 200 and 250 nm.

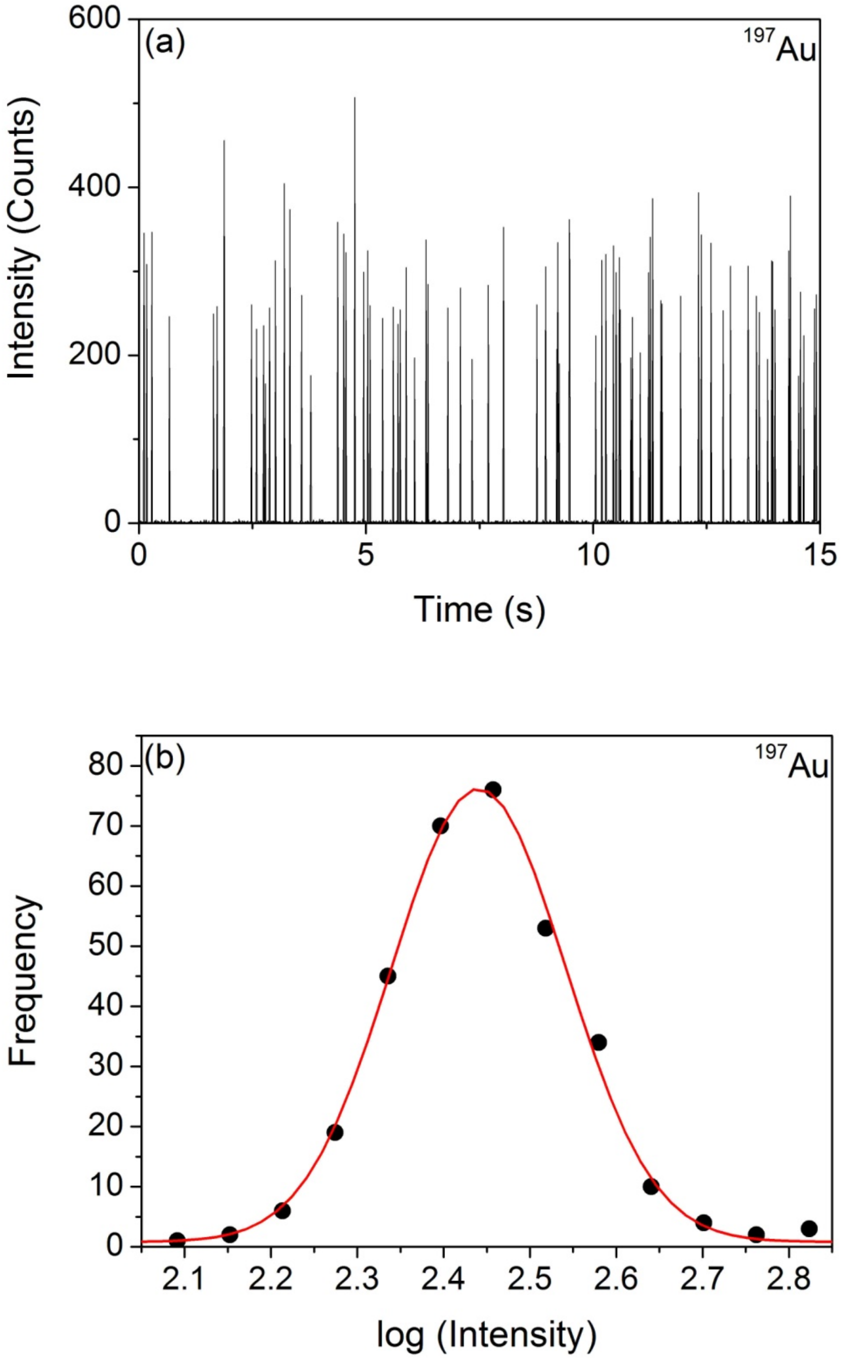

Figure 1. (a) ICP-MS temporal profile of ^{197}Au of the 100-nm gold nanoparticles. (b) ICP-MS intensity distribution of the particles. (ICP forward power = 1400 W, central channel gas flow rate = 1.05 L/min, sampling depth = 6 mm, particle number density = 10^4/mL).

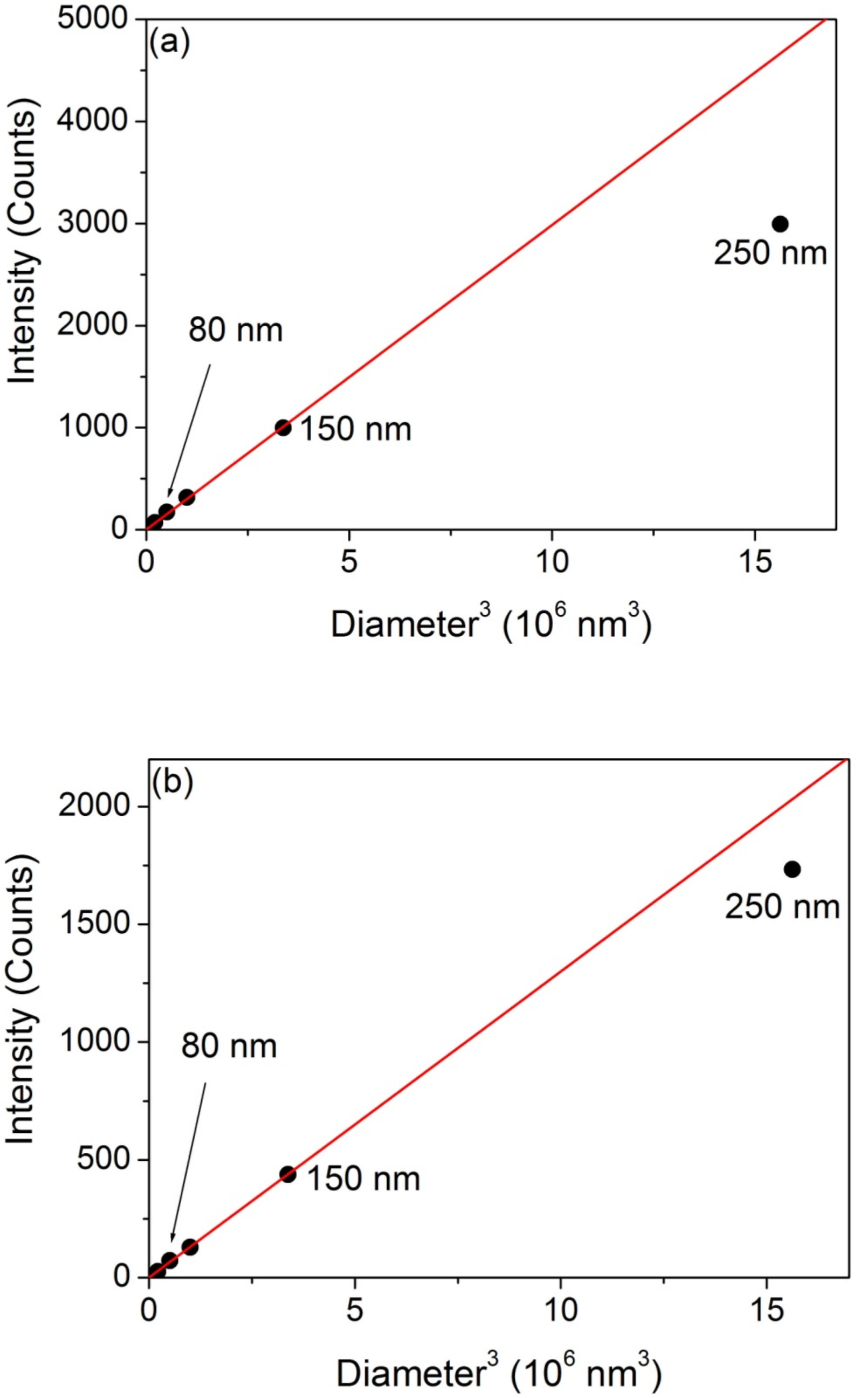

Figure 2. Calibration curves of gold nanoparticles of diameter of 60, 80, 100, 150 and 250 nm at sampling depth (a) 7 mm and (b) 12 mm. Forward power = 1400 W and central channel gas flow rate = 0.95 L/min.

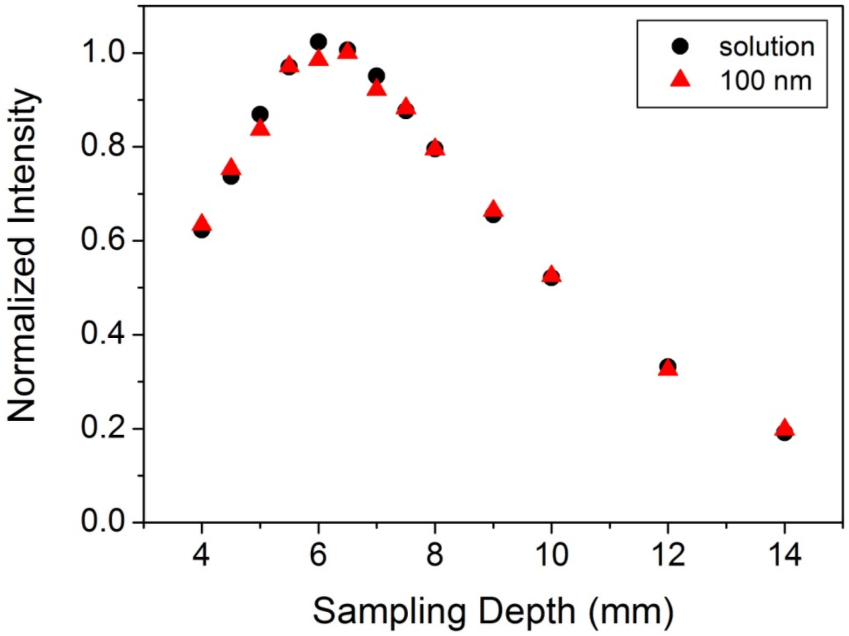

Figure 3. Depth profiles of normalized intensity of gold standard solution and 100-nm gold nanoparticles. (ICP forward power = 1400 W, central channel gas flow rate = 1.05 L/min).

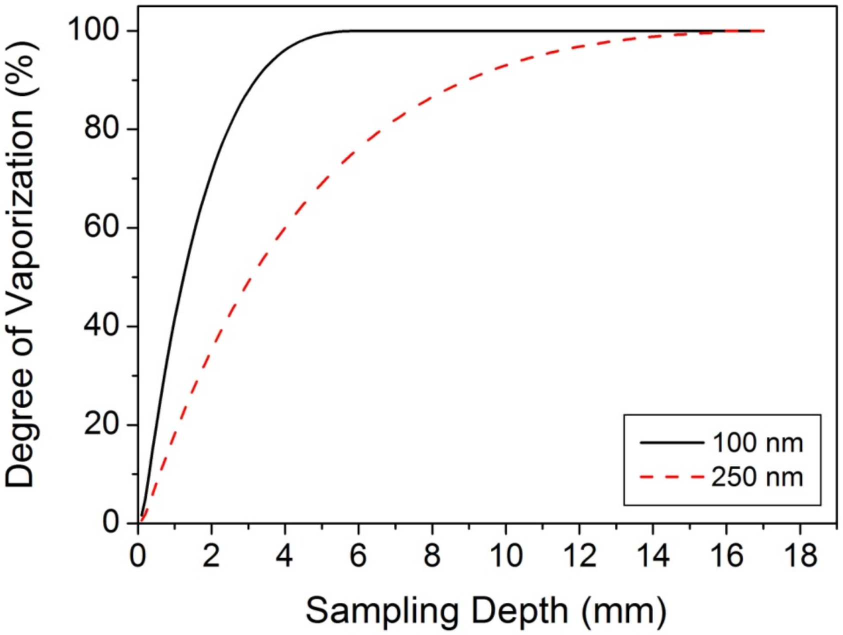

Figure 4. Degree of vaporization against sampling depth for the 100-nm and 250-nm gold nanoparticles. (ICP forward power = 1400 W, central channel gas flow rate = 1.05 L/min).

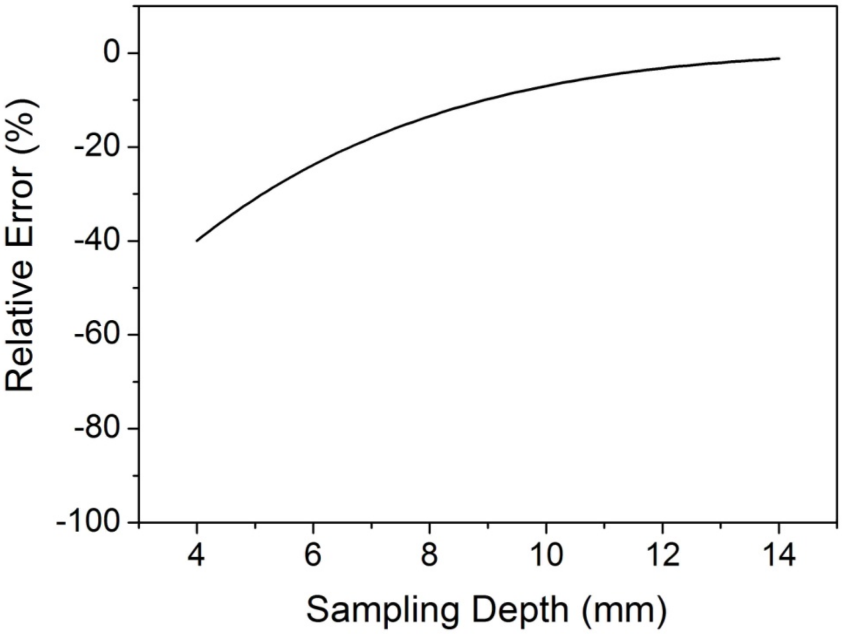

Figure 5. Relative error in calibration due to incomplete vaporization of the 250-nm gold nanoparticle. (ICP forward power = 1400 W, central channel gas flow rate = 1.05 L/min).

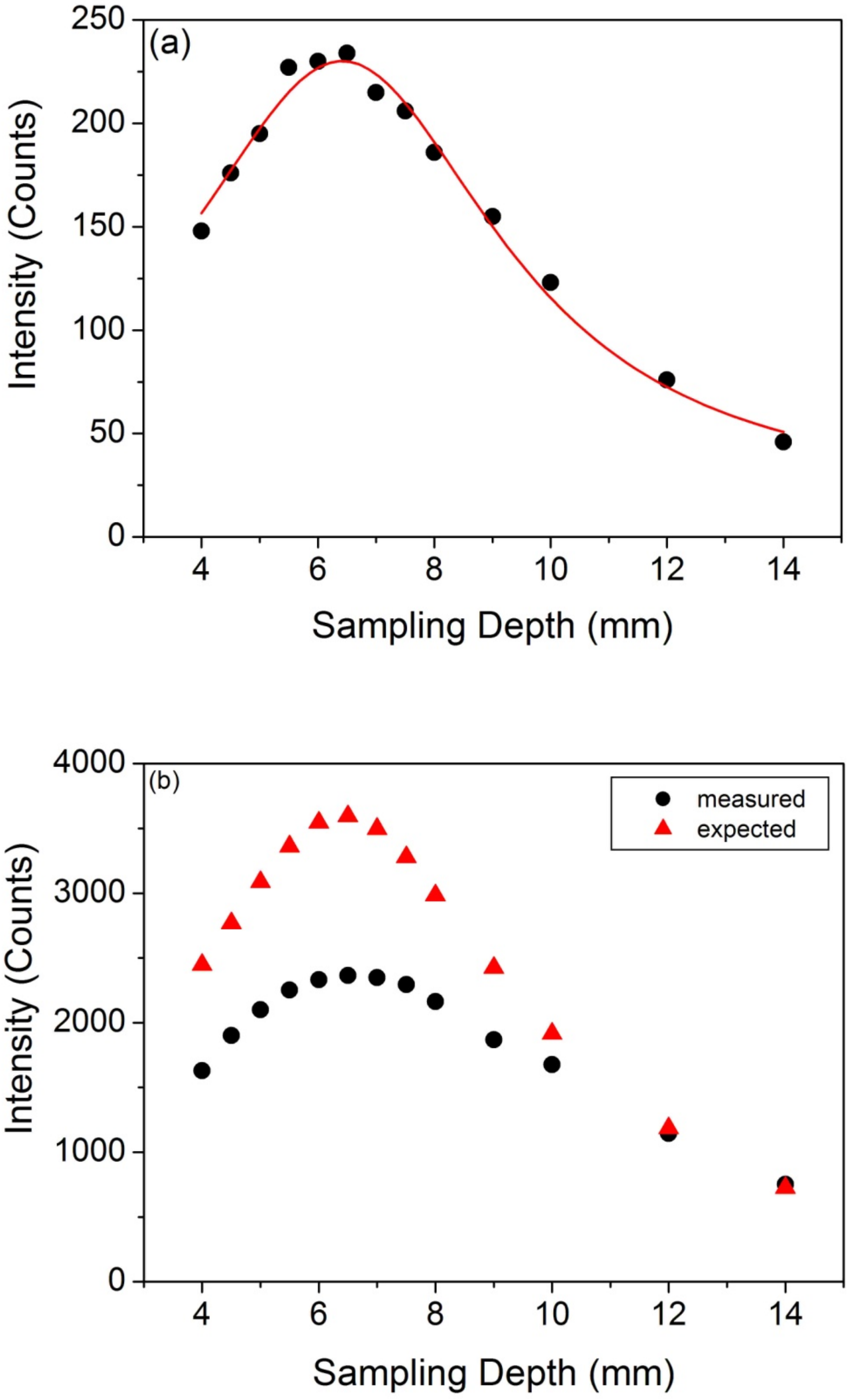
(a)
Intensity (Counts)
250
200
150
100
50
0
4
6
8
10
12
14
Sampling Depth (mm)
(b)
● measured
▲ expected
Intensity (Counts)
4000
3000
2000
1000
0
4
6
8
10
12
14
Sampling Depth (mm)

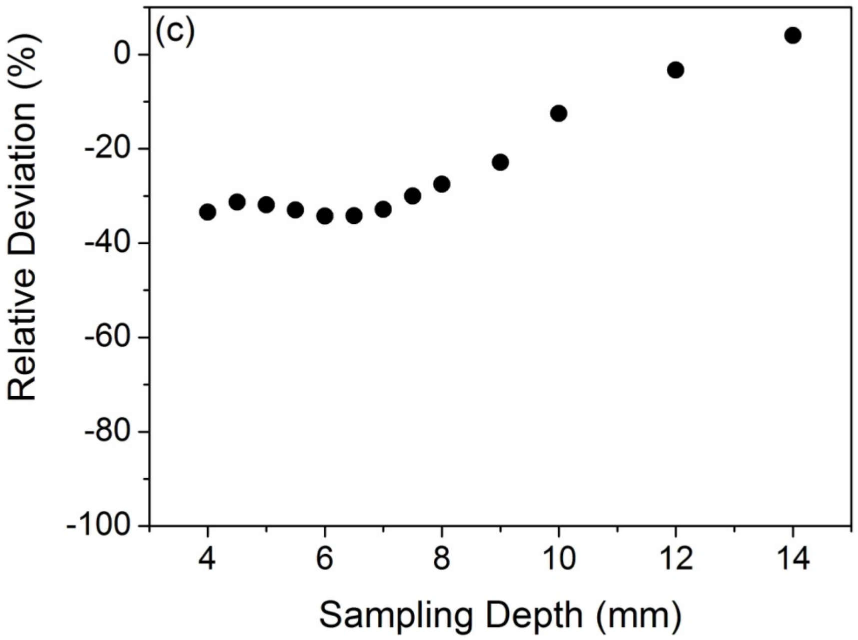

Figure 6. Depth profiles of ICP-MS intensity of (a) 100-nm and (b) 250-nm gold nanoparticles. (c) Relative deviation from linearity of ICP-MS intensity of the 250-nm gold nanoparticles. (ICP forward power = 1400 W, central channel gas flow rate = 1.05 L/min).

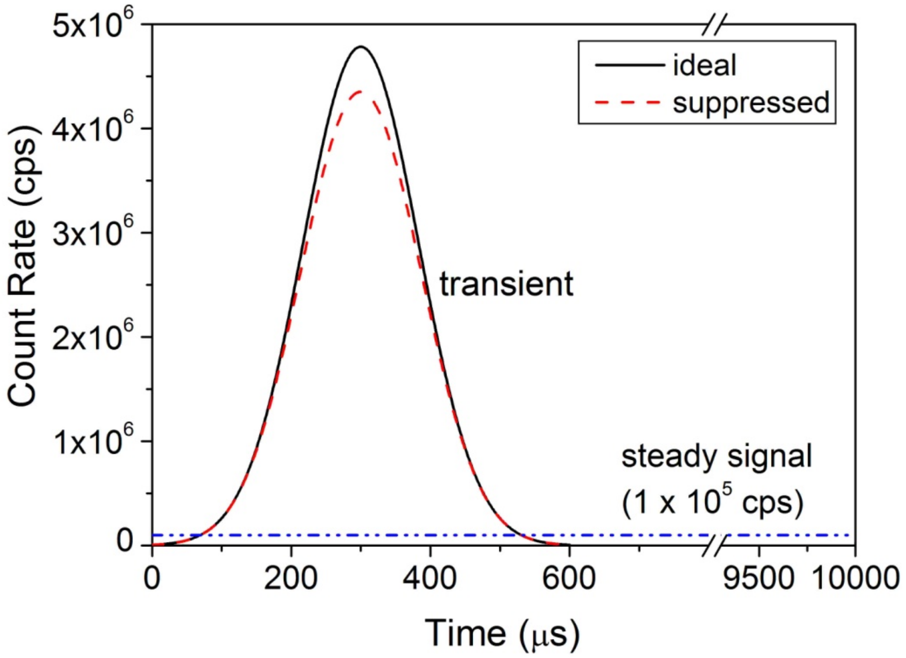

Figure 7. Simulated ideal and suppressed count rates for transient signal of base width of 600 μs and continuous steady signal. Both signals give 1000 counts in the 10-ms integration window. The dead time of the electron multiplier is 40 ns.

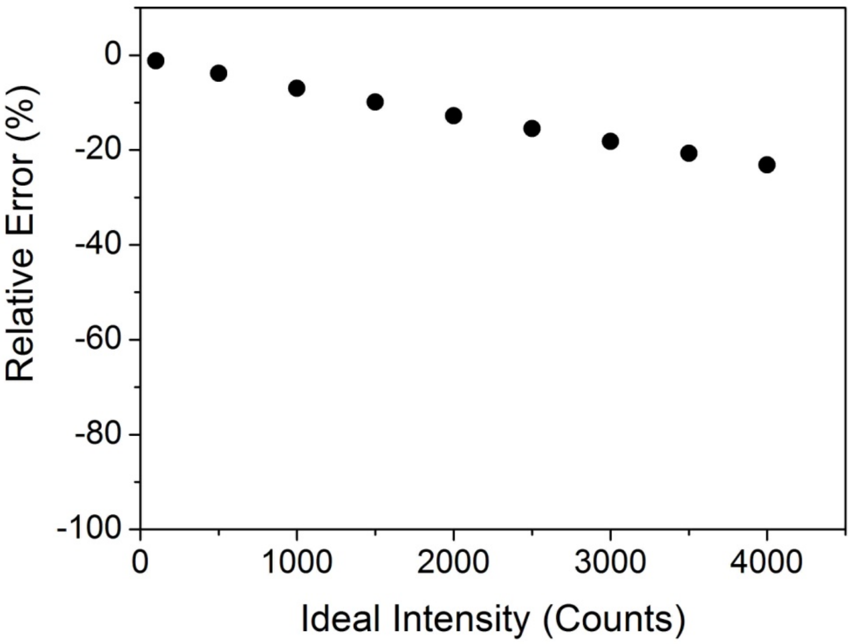

Figure 8. Relative error of the ICP-MS detector operated in digital pulse-counting mode *versus* the intensity of the 600-µs Gaussian transient signal in Figure 7.

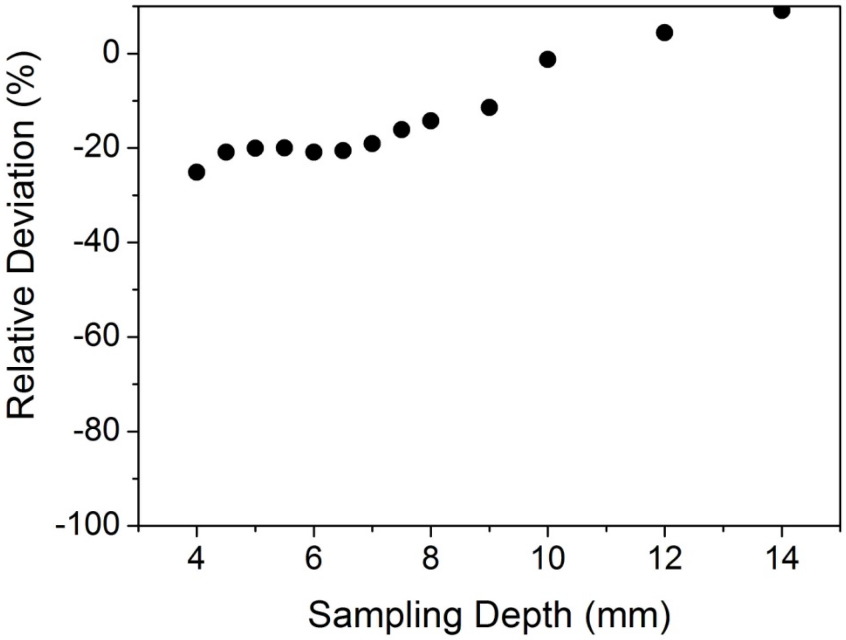

Figure 9. Corrected deviation of ICP-MS intensity of the 250-nm gold nanoparticles. (ICP forward power = 1400 W, central channel gas flow rate = 1.05 L/min).

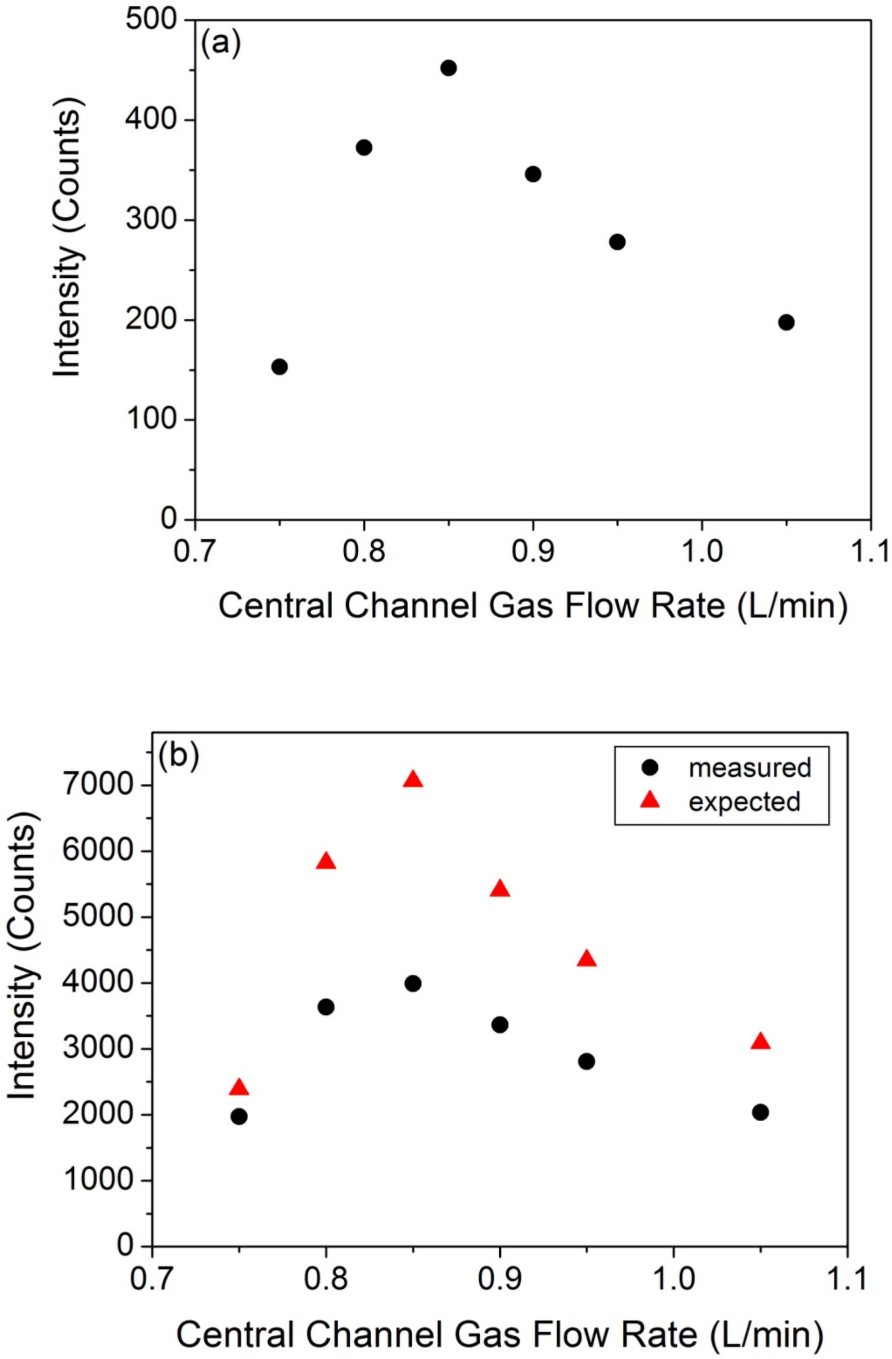
(a)
Intensity (Counts)
0
100
200
300
400
500
0.7
0.8
0.9
1.0
1.1
Central Channel Gas Flow Rate (L/min)
(b)
● measured
▲ expected
Intensity (Counts)
0
1000
2000
3000
4000
5000
6000
7000
0.7
0.8
0.9
1.0
1.1
Central Channel Gas Flow Rate (L/min)

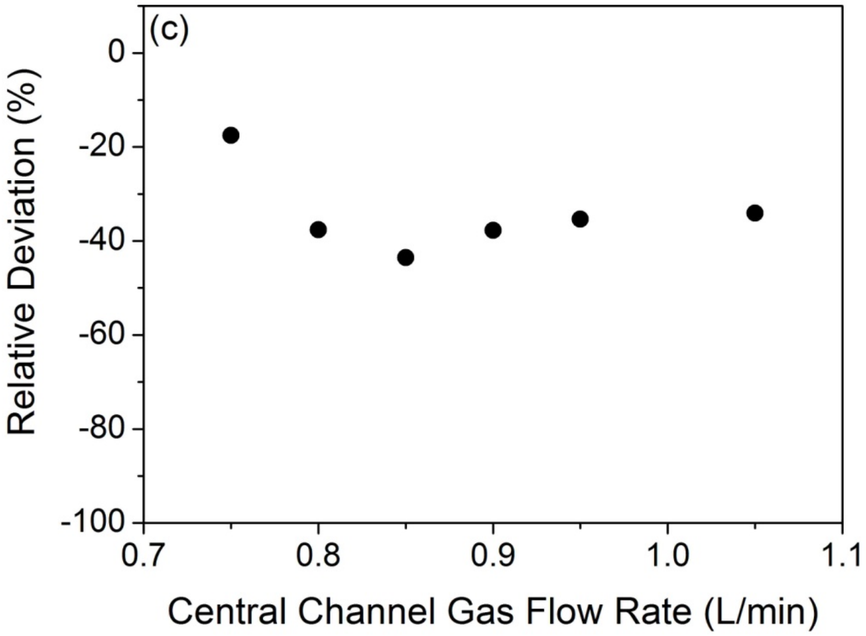

Figure 10. Profiles of SP-ICP-MS intensity *versus* central channel gas flow rate of (a) 100-nm and (b) 250-nm gold nanoparticles. (c) Deviation from linearity of ICP-MS intensity of the 250-nm gold nanoparticles. (ICP forward power = 1400 W, sampling depth = 7 mm).

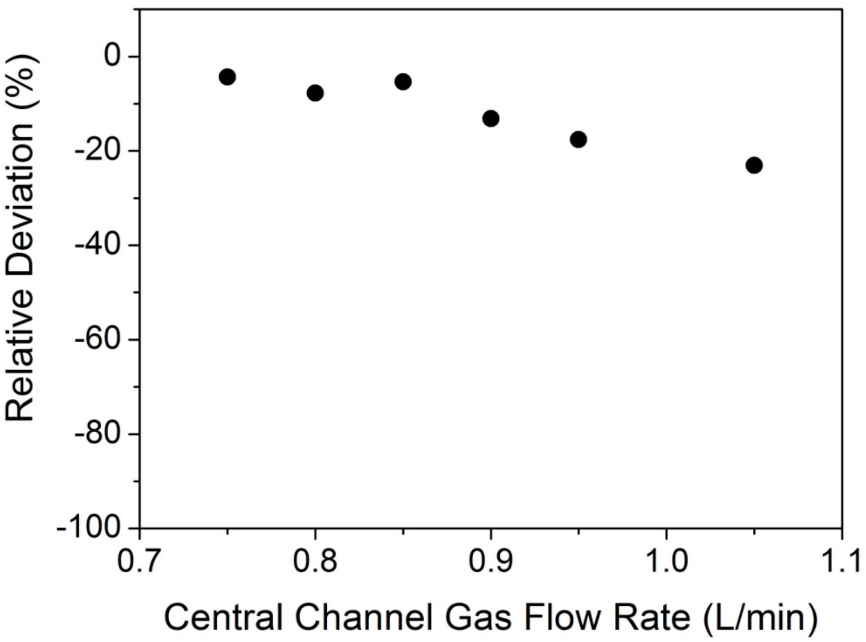

Figure 11. Corrected deviation of ICP-MS intensity of the 250-nm gold nanoparticles *versus* central channel gas flow rate. (ICP forward power = 1400 W, sampling depth = 7 mm).

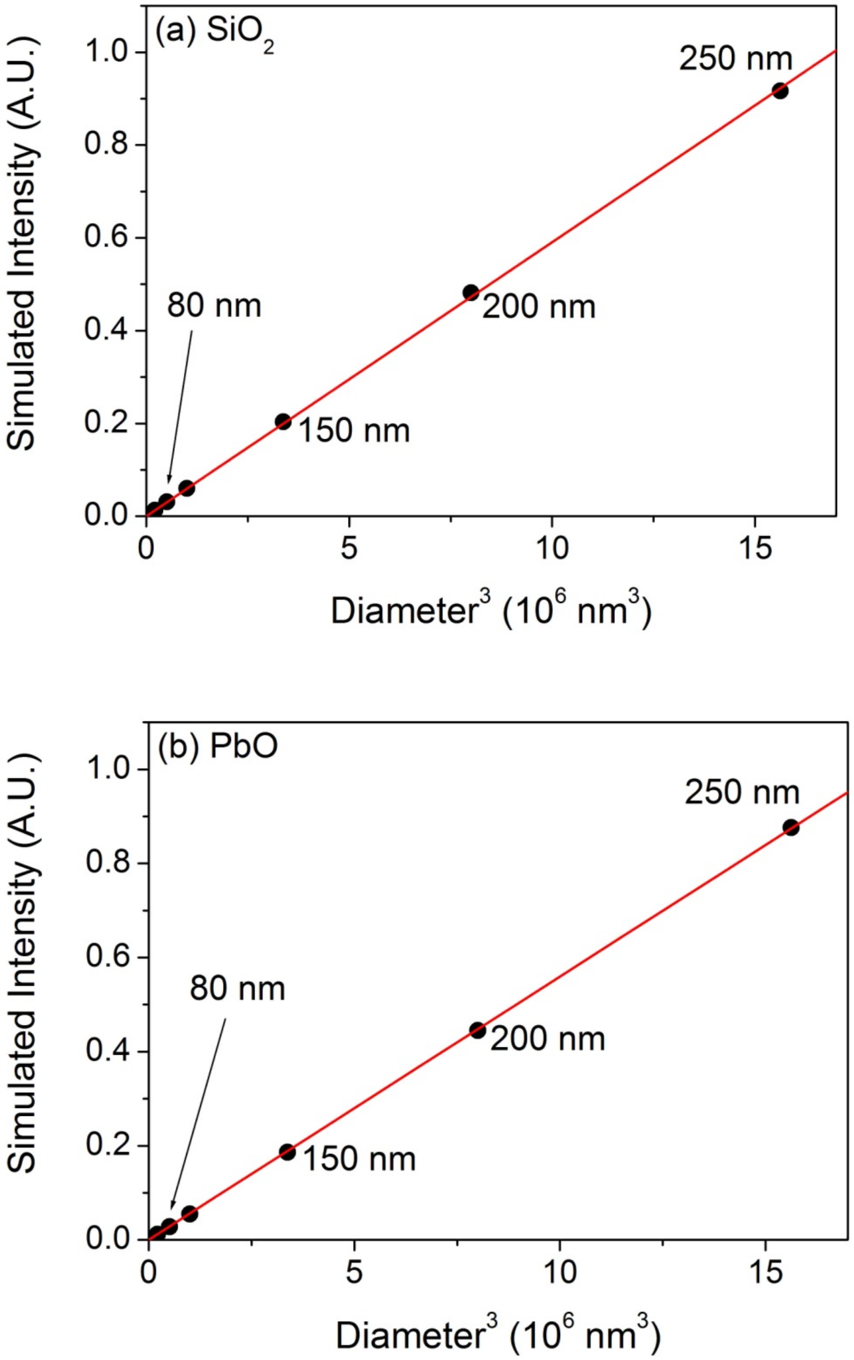
(a) SiO$_2$
Simulated Intensity (A.U.)
1.0
0.8
0.6
0.4
0.2
0.0
250 nm
200 nm
150 nm
80 nm
0
5
10
15
Diameter^3 (10^6 nm^3)
(b) PbO
Simulated Intensity (A.U.)
1.0
0.8
0.6
0.4
0.2
0.0
250 nm
200 nm
150 nm
80 nm
0
5
10
15
Diameter^3 (10^6 nm^3)

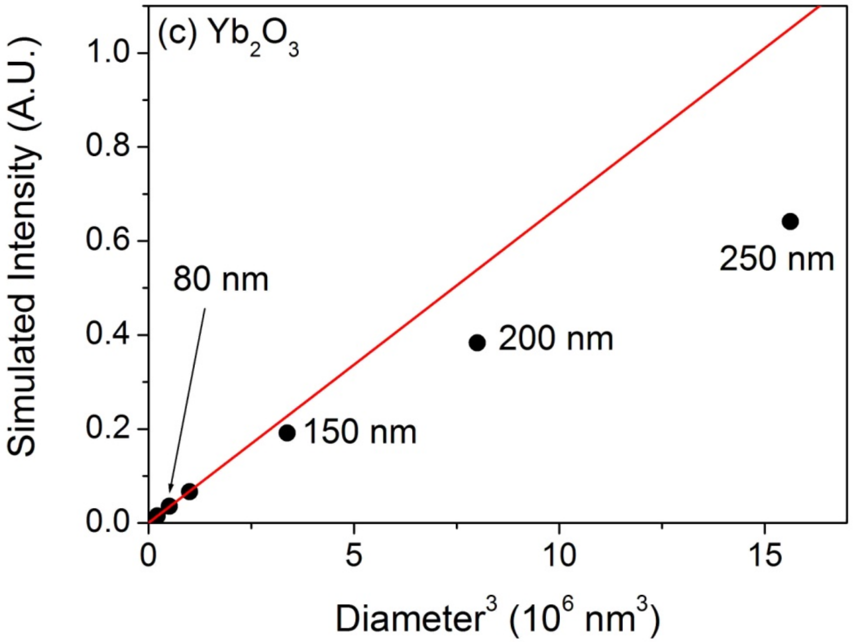

Figure 12. Simulated calibration curves of nanoparticles of (a) SiO_2, (b) PbO and (c) Yb_2O_3. ICP forward power = 1400 W, central channel gas flow rate = 1.05 L/min, and sampling depth = 4 mm. Particle diameter = 60, 80, 100, 150, 200 and 250 nm.

List of Tables

Table

Table 1. Typical operating parameters of the ICP-MS.

ICP forward power	1400 W
Reflected power	< 5 W
RF frequency	27.12 Hz
Plasma gas flow rate (Ar)	15 L/min
Auxiliary gas flow rate (Ar)	1 L/min
Central channel gas flow rate (Ar)	1.05 L/min
Type of nebulizer	V-groove
Spray chamber	Water-cooled Scott-type double-pass
ICP torch injector diameter	1.5 mm
Sample uptake rate	0.4 mL/min
Sampling depth	4 - 14 mm
Sampler aperture	1.0 mm
Skimmer aperture	0.4 mm
Data acquisition mode	Time-resolved analysis (TRA)
Data sampling rate	100 Hz
Measurement duration	60 s

Table 2. SP-ICP-MS calibration methods and experimental errors in literature.

Particles	Analyte	Calibration method	Errors in particle diameter (%)	Errors in analyte content (%)	Reference
Au	Au	Single droplets	< – 1	< – 2*	[22]
Au, Ag	Au, Ag	Single droplets	< – 5*	< – 15	[13]
Mouse fibroblast cell	Ca	Single droplets	20	70*	[29]
Ag	Ag	Standard particles	< – 5	< – 10*	[16]
H. pylori	Mg	Standard particles	< 5	< 10*	[27]
C. vulgaris	Mg	Standard Particles	< 5	< 10*	[7]
C. vulgaris	Mg	Standard solution	– 30	– 70*	[7]
Ag	Ag	Standard solution	– 10 to – 20*	– 30 to – 50	[33]
B. subtilis	U	Standard solution	– 10	– 30*	[10]
Ag	Ag	Standard solution	– 10 to – 20*	– 30 to – 50	[20, 21]
Au	Au	Standard solution	– 30	– 70*	[37]
PbO	Pb	Standard solution	> – 10	> – 30*	[6]

* Errors reported in the literature. The other errors are calculated from the reported values.

Table 3. Properties of SiO_2, PbO and Yb_2O_3 [41].

Particle type	Density (g/cm^3)	Molecular weight (g/mol)	Boiling point (K)	Linear range (nm)
Au	19.3	196.97	3129	≤ 150
SiO_2	2.65	60.08	2863	≥ 250
PbO	9.35	223.20	1750	≥ 250
Yb_2O_3	9.17	394.08	4343	≤ 100